ACCOUNTS
of chemical research

Ruthenia-Based Electrochemical Supercapacitors: Insights from First-Principles Calculations

VIDVUDS OZOLIŅŠ,*,† FEI ZHOU,† AND MARK ASTA‡

†*Department of Materials Science and Engineering, University of California, Los Angeles, P.O. Box 951595, Los Angeles, California 90095-1595, United States, and* ‡*Department of Materials Science and Engineering, University of California at Berkeley, Berkeley, California 94720-1760, United States*

RECEIVED ON NOVEMBER 2, 2012

CONSPECTUS

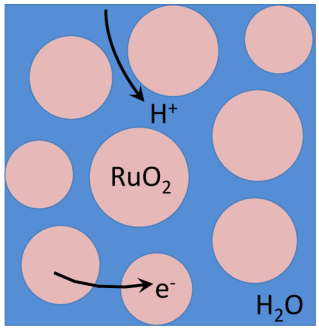

Electrochemical supercapacitors (ECs) have important applications in areas where the need for fast charging rates and high energy density intersect, including in hybrid and electric vehicles, consumer electronics, solar cell based devices, and other technologies. In contrast to carbon-based supercapacitors, where energy is stored in the electrochemical double-layer at the electrode/electrolyte interface, ECs involve reversible faradaic ion intercalation into the electrode material. However, this intercalation does not lead to phase change. As a result, ECs can be charged and discharged for thousands of cycles without loss of capacity. ECs based on hydrous ruthenia, $RuO_2 \cdot xH_2O$, exhibit some of the highest specific capacitances attained in real devices. Although RuO_2 is too expensive for widespread practical use, chemists have long used it as a model material for investigating the fundamental mechanisms of electrochemical supercapacitance and heterogeneous catalysis.

In this Account, we discuss progress in first-principles density-functional theory (DFT) based studies of the electronic structure, thermodynamics, and kinetics of hydrous and anhydrous RuO_2. We find that DFT correctly reproduces the metallic character of the RuO_2 band structure. In addition, electron−proton double-insertion into bulk RuO_2 leads to the formation of a polar covalent O−H bond with a fractional increase of the Ru charge in delocalized *d*-band states by only 0.3 electrons. This is in slight conflict with the common assumption of a Ru valence change from Ru^{4+} to Ru^{3+}. Using the prototype electrostatic ground state (PEGS) search method, we predict a crystalline RuOOH compound with a formation energy of only 0.15 eV per proton. The calculated voltage for the onset of bulk proton insertion in the dilute limit is only 0.1 V with respect to the reversible hydrogen electrode (RHE), in reasonable agreement with the 0.4 V threshold for a large diffusion-limited contribution measured experimentally. DFT calculations also predict that proton diffusion in RuO_2 is hindered by a migration barrier of 0.8 eV, qualitatively explaining the observed strong charging rate-dependence of the diffusion-limited contribution. We found that reversible adsorption of up to 1.5 protons per Ru on the (110) surface contributes to the measured capacitive current at higher voltages. PEGS-derived models of the crystal structure of hydrated ruthenia show that incorporation of water in Ru vacancies or in bulk crystals is energetically much more costly than segregation of water molecules between slabs of crystalline RuO_2. These results lend support to the so-called "water at grain boundaries" model for the structure of hydrous $RuO_2 \cdot xH_2O$. This occurs where metallic nanocrystals of RuO_2 are separated by grain boundary regions filled with water molecules. Chemists have attributed the superior charge storage properties of hydrous ruthenia to the resulting composite structure. This facilitates fast electronic transport through the metallic RuO_2 nanocrystals and fast protonic transport through the regions of structural water at grain boundaries.

1. Introduction

Electrochemical capacitors (ECs), or supercapacitors, occupy an intermediate territory between batteries and conventional capacitors by combining high power density with high energy density.[1] Due to their much faster response times and better cycle life in comparison with conventional batteries, they find numerous applications where high power is in premium over high energy density, such as in hybrid and electric vehicles, energy recovery (e.g., regenerative braking), consumer electronics, and solar cell based devices.[2] Supercapacitors differ from batteries in several aspects. First, they display an approximately linear relationship

Published on the Web 04/05/2013 www.pubs.acs.org/accounts
10.1021/ar3002987 © 2013 American Chemical Society

between the voltage and the amount of stored charge, in contrast to the approximately constant voltage behavior of batteries. Second, the ECs show approximately rectangular current–voltage curves, while batteries exhibit sharp peaks corresponding to faradaic redox reactions. Finally, the ECs store energy via fast and reversible surface or near-surface processes, bypassing bulk phase transformations which limit the charging rates of batteries.[1]

Currently, the most widespread type of EC uses high-surface area carbon electrodes where energy is stored in the electrochemical double-layer at the carbon/electrolyte interface. Since carbon double-layer ECs are limited in their specific capacitance to maximum values of approximately 150 F/g, there is strong interest in developing ECs where energy is stored by adsorbing or intercalating ions into the electrode material and realizing reversible redox reactions. Ruthenium dioxide, RuO_2, is a prototypical EC electrode material with one of the highest specific energy densities of all known materials (almost 800 F/g in hydrous RuO_2).[3,4] RuO_2 is a rare stoichiometric oxide which combines chemical and thermal stability, metallic conductivity, and redox activity with good catalytic properties.[5,6]

We start by reviewing the history and the current understanding of the mechanism of supercapacitance in RuO_2. Trasatti and Buzzanca[7] were the first to note that the rectangular current–voltage characteristics of RuO_2 in aqueous electrolyte (typically, 0.5 M sulfuric acid) resembled those of carbon supercapacitors and hypothesized that charge storage occurs via the electronic-protonic double insertion reaction:

$$RuO_x(OH)_y + \delta e^- + \delta H^+ \leftrightarrow RuO_{x-\delta}(OH)_{y+\delta} \qquad (1)$$

They also proposed that the valence state of Ru can change from Ru^{4+} to Ru^{3+} and even Ru^{2+}. The rectangular shape of the voltammogram was attributed to the existence of a wide energy distribution for the adsorbed protons. This is an important difference from batteries, which typically have only a few distinct adsorption sites and involve bulk phase transformations (e.g., $Li^+ + e^- + CoO_2 \leftrightarrow LiCoO_2$).

Using electrochemical measurements, Ardizzone et al.[8] inferred that two types of sites exist in RuO_2: inner (less accessible) and outer (more accessible) surface sites. Proton adsorption at the inner sites shows an inverse square root dependence on the charging rate characteristic for diffusion processes, while the outer sites exhibit rate-independent charging usually associated with pure surface processes, such as double-layer contributions or reversible surface protonation. The outer adsorption sites give rise to the rectangular voltammogram which served as the basis for the original proposal of Trasatti and Buzzanca.[7] Later studies have shown that nanocrystalline films of RuO_2 exhibit a significant rate-dependent charging capacity below 0.4 V with respect to the reversible hydrogen electrode (RHE), which is attributed to proton intercalation along the grain boundaries.[4]

An important breakthrough was achieved by Zheng et al.,[9] who demonstrated that hydrous ruthenia, $RuO_2 \cdot xH_2O$, shows significantly higher charging rate and specific capacity than nanocrystalline anhydrous RuO_2. The superior performance of hydrous ruthenia is usually attributed to its mixed protonic–electronic conductivity. Indeed, it has been shown that $RuO_2 \cdot xH_2O$ with optimal water content ($x \approx 0.5$) does not exhibit significant amounts of the slow inner site adsorption, in marked contrast to nanocrystalline films of anhydrous RuO_2.[4] The rate of proton diffusion was measured by Fu et al.,[10] who found that the activation energy is low for the $RuO_2 \cdot xH_2O$ samples annealed in the temperature range of 116–175 °C, but relatively high for those annealed below 100 °C or above 200 °C. These studies are in line with capacitance measurements, which also indicate that intermediate annealing temperatures lead to the best performance, pointing to the importance of nanoscale structure control of hydrous $RuO_2 \cdot xH_2O$ for the mechanisms of supercapacitance.[11]

Structural studies of $RuO_2 \cdot xH_2O$ are complicated by its apparent amorphous-like structure and lack of detailed information about the atomic positions. Two models were critically examined by McKeown et al.[3] using a combination of characterization techniques. The first model assumed that water molecules are incorporated in ruthenium vacancies in the bulk material either as H_2O or as OH^- and H^+, resulting in interconnected chains of highly disordered RuO_6 octahedra. We call this the "water in bulk vacancies" model, and it is schematically shown in Figure 1a. The second model assumed that water is dispersed between RuO_2 nanocrystals, and the material can be best described as an RuO_2/H_2O composite held together by boundary layers of structural water. The grain boundaries are believed to be permeable to protons, constituting an enormous inner surface area and therefore leading to high capacitance. A subsequent study by the same group[11] used X-ray scattering to demonstrate that the structure of $RuO_2 \cdot xH_2O$ is best described by the second model. These authors also noted that the "water at grain boundaries" model naturally explains the observed charge-storage properties of hydrous ruthenia in terms of percolating networks of electronic and protonic conduction

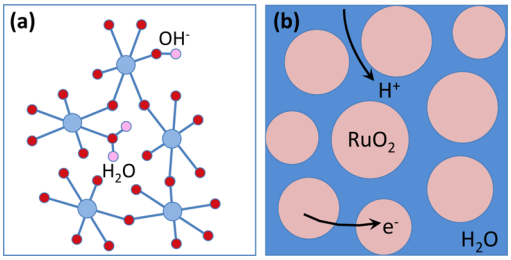

FIGURE 1. Schematic structural models proposed for $RuO_2 \cdot xH_2O$: (a) "water in bulk vacancies" and (b) "water at grain boundaries". Ruthenium, oxygen, and hydrogen ions are shown as blue, red, and pink circles, respectively.

pathways, as shown in Figure 1b: the hydrous regions serve as proton conduction pathways, but are relatively impermeable for electrons, while the RuO_2 nanocrystals are electrically conductive, but impermeable to protons. Too much water at the boundaries decreases electronic transport, while too little water decreases proton transport. Peak performance results when the rates of proton and electron conduction are balanced.

Even though the "water at grain boundaries" model has gained general acceptance,[4,12−14] many fundamental questions remain unsettled. For instance, there is only a rudimentary understanding of the atomic-level mechanisms that lead to nearly rectangular current−voltage curves. The capacitive contribution from surface redox reactions is still unclear, mostly due to the difficulty of distinguishing surface pseudocapacitance from the double layer capacitance. Proton intercalation energetics in bulk RuO_2 and the kinetic barriers to proton diffusion are poorly understood, and open questions remain about the structure and thermodynamic stability of hydrous $RuO_2 \cdot xH_2O$, in particular regarding the structure and properties of intergranular water. This Account presents a brief review of our research into RuO_2-based materials using modern first-principles density functional theory (DFT) calculations and also serves as a basic introduction into first-principles modeling of the physical and chemical properties of aqueous ECs.

2. Electronic Structure of RuO_2

RuO_2 crystallizes in the tetragonal rutile structure shown in Figure 2. Each ruthenium atom is octahedrally coordinated to six oxygen atoms. The structure can be viewed as consisting of chains of edge-sharing RuO_6 octahedra running along the 4-fold [001] axis; octahedra of neighboring chains share corners. The octahedra are slightly distorted in the tetragonal direction so that the lengths of the shared O−O edges (along [110]) are 2.47 Å, the two edges along the chain

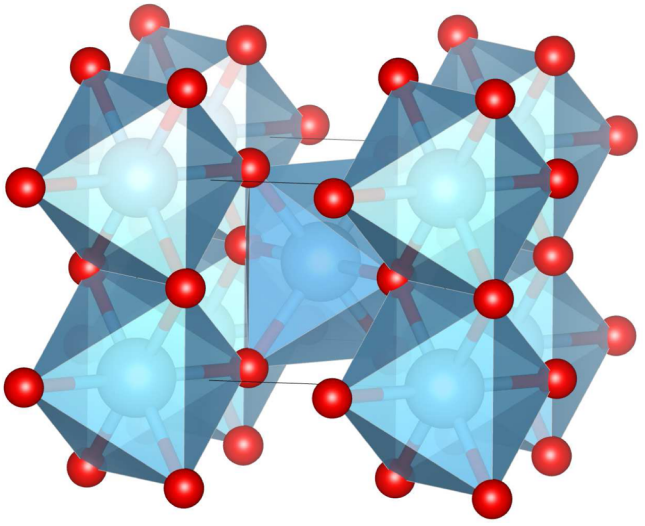

FIGURE 2. Bulk crystal structure of RuO_2. Tetragonal *z* axis is oriented along the vertical direction.

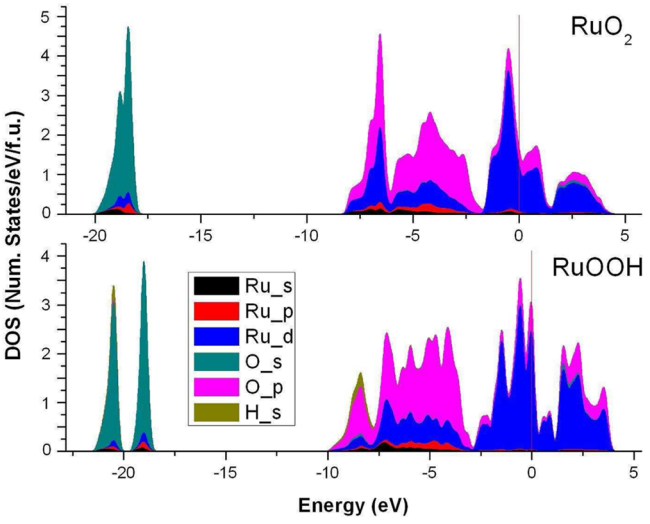

FIGURE 3. Calculated atom- and orbital-decomposed eDOS for RuO_2 and RuOOH. The Fermi level is at zero energy.

direction [001] are elongated to 3.11 Å, and the remaining eight O−O distances are 2.78 Å. These distances are comparable to typical O−O distances in ice (approximately 2.8 Å), suggesting that hydrogen bonding plays an important role in determining the energies and crystallographic positions of intercalated protons.

The calculated electronic density-of-states (eDOS) in Figure 3, obtained using the generalized gradient approximation (GGA), is metallic.[15] The filled lower-lying valence bands between −8 and −2 eV are bonding hybrids of O 2*p* and Ru 4*d* orbitals, while the states near the Fermi level are of predominantly Ru 4*d* character, formed by overlapping Ru 4*d* orbitals across the shared edges of RuO_6 octahedra.[16]

TABLE 1. Calculated Bader Charges for Bulk RuO_2 and Hypothetical Electron-Proton Double-Inserted RuOOH[a]

compd	atom	Bader charge	total
RuO_2	Ru	6.4	+1.6
	O	6.8	−0.8
RuOOH	Ru	6.7	+1.3
	O1	7.0	−1.0
	O2	6.9	−0.9
	H	0.4	+0.6

[a]The last column gives the total ionic charge including nuclear contribution.

It is commonly accepted that electron−proton double insertion [eq 1] adds electrons to Ru 4*d* orbitals and causes valence change from Ru^{4+} to Ru^{3+}. However, this assertion should be treated with some skepticism because RuO_2 is a metallic compound where electrons at the Fermi level are spatially delocalized, and hence the added electron is unlikely to reside on one particular Ru ion. We examine this issue in more detail by studying a hypothetical RuOOH compound where one hydrogen has been inserted per formula unit. The resulting eDOS in Figure 3 shows that strong hybridization occurs between the oxygen 2*p* and hydrogen 1*s* orbitals, suggesting a polar covalent O−H bond, accompanied by noticeable changes in the eDOS near the Fermi level. The calculated Bader charges[17] are compared in Table 1. While the formal valence of Ru is 4+, the calculated Bader charge for Ru in RuO_2 is +1.6, lower than the value of +1.9 calculated for Ti in TiO_2,[18] which we attribute to the higher electronegativity of Ru (2.2 vs 1.54 for Ti). After hydrogen insertion, the Ru ions acquire additional 0.3 electrons; the remaining 0.7 electrons are divided between the proton (0.4) and the two types of oxygen ions (with 0.2 electrons going to the oxygen that bonds the proton). These results suggest that the added electrons are distributed between the OH bond and extended metallic Ru 4*d* states, and challenge the commonly held view that proton insertion leads to a well-defined change in the oxidation state of Ru. This conclusion is further supported by the calculated charge distribution of the inserted electron in Figure 4, obtained as the valence charge density difference between RuOOH and RuO_2. It is clear that the extra electron is mainly confined around the hydroxyl group and affects the charge density around the Ru atoms by a small amount.

3. Voltage Calculations

In this section, we are concerned with the thermodynamics of proton intercalation and surface adsorption. We adopt RHE as a reference electrode in thermodynamic equilibrium

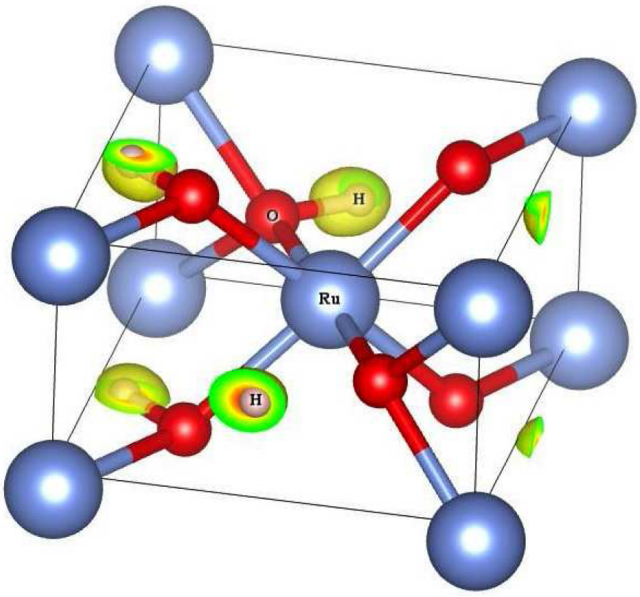

FIGURE 4. Charge density distribution of an extra electron in RuOOH relative to RuO_2. To facilitate the comparison, the atoms in RuO_2 are fixed to their positions in RuOOH.

with hydrogen gas. Voltages corresponding to proton intercalation are given by[19]

$$V_n = -\frac{\Delta G(n+1) - \Delta G(n)}{e} \qquad (2)$$

where n is the number of intercalated protons, e is the electronic charge, and the free energies are calculated with respect to gas-phase hydrogen molecules:

$$\Delta G(n) = G[RuO_2, n] - G[RuO_2] - \frac{n}{2} G^\circ[H_2] \qquad (3)$$

Here, $G[RuO_2,n]$ is the total free energy of RuO_2 (bulk or surface) with n double-inserted protons and electrons, $G[RuO_2]$ is the free energy of RuO_2 before insertion, and $G^\circ[H_2]$ is the standard state free energy of hydrogen gas:

$$G^\circ[H_2] = E_0 + E_{ZPE} + \frac{7}{2} k_B T^\circ - T^\circ S^\circ \qquad (4)$$

where E_0 is the calculated static energy of a hydrogen molecule, E_{ZPE} is the zero-point vibrational energy of H_2 (0.27 eV), and S° = 130.68 J/(mol K) is the entropy of gaseous H_2 at p = 1 bar pressure and temperature T° = 298 K.[20] The zero-point energy (ZPE), enthalpy, and entropy contributions to eq 4 largely cancel, resulting in a small (−0.04 eV/H_2) correction to the static energy. To this, we add the vibrational energy of H in hydroxyl groups formed upon intercalation or surface adsorption. We calculate frequency values of 2800 and 1100 cm^{-1}

for the bond-stretching and rotational hydrogen modes, respectively, resulting in an overall ZPE of 0.3 eV per proton. Furthermore, the proton free energy is a function of pH, $\Delta G_{pH} = k_B T \ln(10^{pH})$, but this contribution is negligible for 0.5 M H_2SO_4 (pH = 0.3).

The stability of a given surface structure with n_O oxygen ions and n_H protons under external potential V_{ext} is determined by its surface free energy:

$$\Delta G_{surf}(n_O, n_H) = G(n_O, n_H) - n_O(\mu_{H_2O} - 2\mu_H) - n_H\mu_H \quad (5)$$

where μ_{H_2O} is the chemical potential of water, given by eq 9 below, and μ_H is the chemical potential of hydrogen; we assume equilibrium between the water and the adsorbed O and H species. If the external potential V_{ext} is measured relative to the onset voltage for H_2 release, μ_H can be expressed as

$$\mu_H = \frac{1}{2} G^{\circ}[H_2] - V_{ext} \quad (6)$$

where V_{ext} accounts for the energy to transfer an electron during $2H_3O^+ + 2e^- \leftrightarrow H_2 + 2H_2O$. The most stable surface structure at a given V_{ext} minimizes eq 5, and voltages where the proton (n_H) and/or oxygen (n_O) coverages change correspond to peaks in voltammetry curves.

4. Protons in Bulk RuO_2

We first investigate the stability of bulk hydroxide, $Ru(OH)_2$, and oxyhydroxide, RuOOH. While neither has been characterized experimentally, these hypothetical compounds may play a role in the charge storage properties of RuO_2. Predicting crystal structures from the first principles remains a very challenging task even for relatively simple systems. We applied the prototype electrostatic ground state (PEGS) method, which was specifically designed for predicting crystal structures of ionic compounds and nanoclusters.[21,22] The PEGS method assumes that the structure type, symmetry and atomic coordination can be determined from the ionic radii and charges using a total energy model that contains soft-sphere repulsion and electrostatic terms. Complex anions and cations, such as OH^- and H^+, are treated as rigid units with positional and orientational degrees of freedom, and the crystal structures are optimized via an efficient search algorithm based on the flat-histogram Wang–Landau Monte Carlo (WLMC) method,[23] which can efficiently jump out of local energy minima and search the entire configuration space. The PEGS algorithm is run for a range of ionic radii and charges, and the resulting structures are fully relaxed using DFT calculations. The structure with the lowest DFT total energy is selected as the candidate ground state.

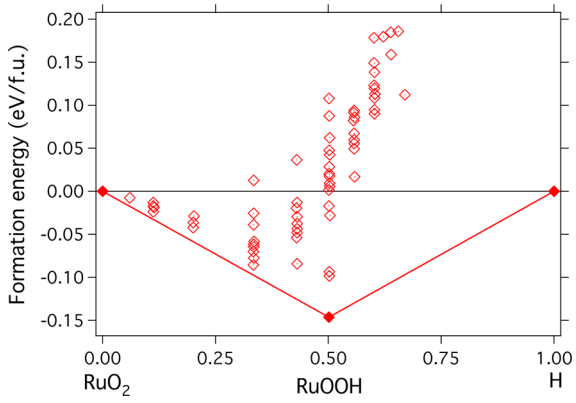

FIGURE 5. Calculated DFT formation energies [eq 3] of ordered $(RuO_2)_{1-x}H_x$ compounds. Line marks the ground state convex hull corresponding to stable structures at $T = 0$ K.

In PEGS runs, we fixed Ru and O atoms at their positions in RuO_2 and kept the O–H bond length and H–O–H bond angle at 0.98 Å and 104.5°, respectively. The allowed configurational changes included rotations and swapping of anions, i.e., hydrogen was allowed to hop and bond to different oxygens. Figure 5 shows the calculated DFT formation energies of various $(RuO_2)_{1-x}H_x$ compounds versus the composition x. The T = 0 K ground-state convex hull is outlined by a continuous line, showing that RuOOH is predicted to be the only stable mixed compound. This compound is more stable than a 1:3:2 mixture of Ru, RuO_2, and H_2O by about 0.04 eV per formula unit at $T = 0$ K; accounting for the entropy of water suggests that RuOOH becomes unstable at room temperature in an aqueous environment.

In the dilute limit, we calculate an electron–proton double-insertion voltage of 0.1 V, which is below the experimentally measured 0.4 V onset of the rate-dependent (presumably, diffusion-controlled) pseudocapacitance in anhydrous RuO_2. Proton diffusion rates in RuO_2 were calculated[15] using the climbing image nudged elastic band method.[24] The shortest O–O pairs are only 2.47 Å apart (red lines in Figure 6A), but they do not form a linked continuous network, and jumps over the second-shortest O–O pairs 2.78 Å apart (blue lines in Figure 6) are needed for long-range diffusion. The O–O distances along the 4-fold axis (parallel to the dense RuO_6 chains) are above 3.1 Å, and direct proton jumps between these oxygen ions are not favored because they require complete breaking of O–H bonds. The calculated migration energy barriers are shown in Figure 6. Along the diffusion path, the O–H bond is

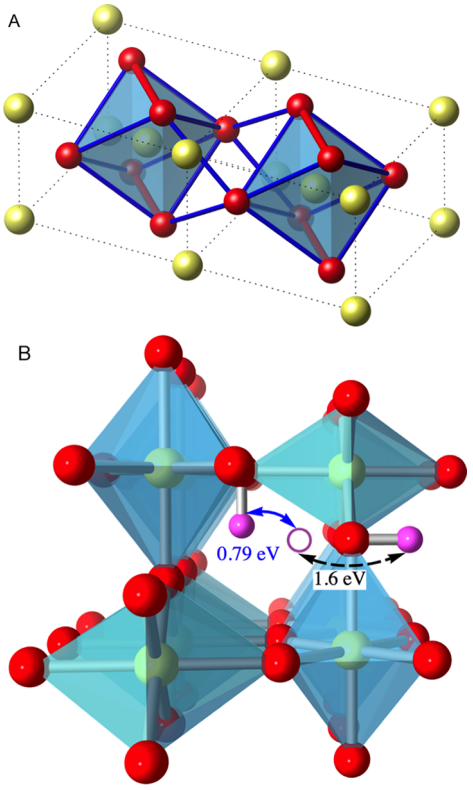

FIGURE 6. Proton diffusion in RuO_2. (A) Distinct types of proton jumps are shown as red and blue lines. (B) A possible proton jump inside the 4-fold channel is marked by a solid blue arrow, while a jump into the neighboring channel is marked by a dashed black arrow.

broken, which results in a barrier of approximately 0.8 eV for jumps indicated by the solid blue arrow in Figure 6. The O−H bond is restored when the target oxygen is approached resulting in an equivalent configuration where the proton has displaced by distance c/2 = 1.55 Å inside the open 4-fold symmetric channel parallel to the tetragonal axis. The diffusion is one-dimensional because proton rotation (indicated by a dashed black arrow in Figure 6) is needed to transfer to a neighboring channel. Due to the strong orientational preference, this rotation results in a migration energy of approximately 1.6 eV, too high to be overcome at normal experimental conditions. The proton diffusion coefficient along the tetragonal axis can be estimated using the standard formula for tracer diffusion:

$$D_z = \frac{f_H \lambda^2}{6} \exp\left(-\frac{E_a}{k_B T}\right) \quad (7)$$

where f_H is the attempt frequency, $\lambda = c/2$ is the distance covered by one hop, and E_a is the migration energy. Approximating f_H by the frequency of the A_1 mode of H_2O (1595 cm^{-1}), we obtain $D_z \approx 10^{-16}$ cm^2/s at room temperature. Quantum tunneling effects can be

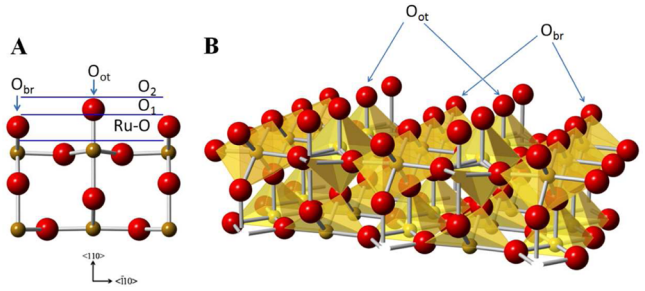

FIGURE 7. Structure of RuO_2(110). The left panel shows possible terminations, and the right panel shows the O-covered surface corresponding to the O2 termination.

estimated using the semiclassical correction developed by Fermann and Auerbach.[25] Using the calculated imaginary frequency at the transition state, 960 cm^{-1}, this correction amounts to a factor of approximately 3 at room temperature. At the slowest sweep rates of 1 mV/s, the classical diffusion distance is approximately 30 Å, or 6 lattice parameters in the *z* direction. For faster voltage sweep rates of 100 mV/s, diffusion distance decreases to 3 Å, showing that proton intercalation into the four-fold channels is limited by diffusion and depends strongly on the charging rate, in qualitative agreement with experimental observations.[3]

5. Proton Adsorption on RuO_2 Surface

Here we discuss contributions to pseudocapacitance arising from surface proton adsorption. Single crystals of RuO_2 typically exhibit (101), (110), and (100) facets, among which (110) is predicted to have the lowest energy.[26] RuO_2(110) has a rectangular surface unit cell and three possible terminating planes: two oxygen-terminated planes (denoted by O2 and O1) and one mixed Ru−O plane, as indicated in Figure 7. Since the O1 surface is stoichiometric and can be grown in ultrahigh vacuum, it is often called ideal RuO_2(110). Several studies indicate that RuO_2(110) should adopt the O2 structure under commonly used experimental conditions, that is, be fully covered by oxygen.[27−29] Our DFT calculations confirm this conclusion.[15] We consider proton adsorption at the on-top (O_{ot}) or bridge site (O_{br}) oxygen ions and require that every OH group points to a nearby oxygen forming a hydrogen bond. Under these constraints, the total number of symmetrically distinct configurations in a 2 × 1 surface unit cell is reasonably small and all possible adsorption configurations in terms of the hydrogen bond orientation and proton coverages can be enumerated. The calculated

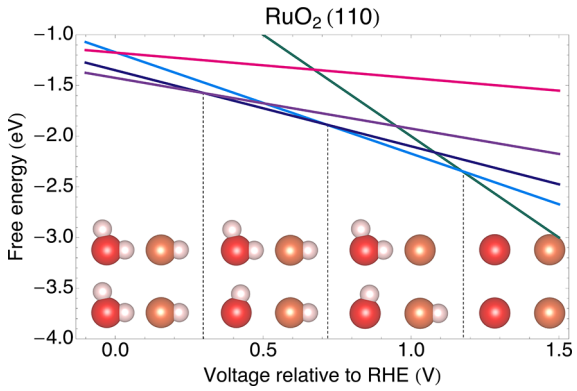

FIGURE 8. Calculated free energies of protonated RuO_2(110) as functions of voltage. Dashed lines denote the position of current peaks due to changing proton coverage, and the inset shows the stable surface structures. On-top oxygen ions (O_{ot}) are red, bridge site oxygens (O_{br}) are orange, and protons are pink. The magenta colored line corresponds to a coverage of 1.75 H/Ru, which is not stable within the considered voltage range.

DFT energies are used in eq 5 to deduce thermodynamic stability and adsorption voltages.

Figure 8 shows ΔG_{surf} for the predicted surface structures near the experimentally accessible voltage range. As expected, RuO_2(110) is gradually deprotonated upon increasing voltage in a series of transitions from 1.5 to 1.25, 1, and 0 adsorbed protons per surface Ru, corresponding to current peaks at approximately 0.3, 0.7, and 1.2 V. Calculations predict that at low potentials one forms water-like groups on O_{ot} sites, and these protons are the first to be desorbed with increasing voltage (around 0.3 V in Figure 8). Upon further increase in V_{ext} to 0.7 V, protons are desorbed from the O_{br} down to a coverage of 1 H/Ru. All the remaining protons are predicted to desorb in a narrow voltage interval around 1.2 V, close to the potential for O_2 evolution.[15] The predicted voltages are in fair agreement with the experimentally measured values of Lister et al.[30] Quantitative discrepancies can be attributed to the errors introduced by the semilocal GGA functional. Self-interaction corrections or hybrid functionals incorporating screened exact exchange are known to yield more accurate predictions for strongly correlated insulators,[31] but it is not clear that they would give more accurate results for a metallic compound such as RuO_2. As an order-of-magnitude estimate, the effect of self-interaction corrections on the formation energy of RuOOH was calculated using the LDA+U scheme,[32] and found to lead to an increase from approximately 0.2 to 0.3, 0.4, 0.5, and 0.8 V for $U_{eff} = U + J$ values of 1, 2, 3, and 4 eV, respectively.[15] In addition, hydrogen bonding with the surrounding water molecules has been neglected here and is expected to further increase desorption voltages. For instance, Nørskov et al.[33] found that OH-covered Pt(111) was stabilized by approximately 0.3 eV/OH in the limit of low coverage. We note that the 1.5 and 1.25 H/Ru structures in Figure 8 are predicted to be metastable because the additional protons favor the subsurface layer.[15] However, it is likely that subsurface intercalation is kinetically inhibited.

In what follows, we discuss the predicted surface structures in more detail. At low proton coverages (below 0.5 H/Ru), the most favorable adsorption sites are at the O_{ot} sites, forming hydrogen bonds with an adjacent O_{ot}.[15] We find that structures where molecular water forms at the O_{ot} sites are competitive, but higher in energy than those with isolated hydroxyl groups. Above 0.5 H/Ru, the protons start to adsorb on the O_{br} sites, forming hydrogen bonds with neighboring O_{ot}. Further increase of proton coverage above 0.75 H/Ru leads to the formation of water-like groups at the O_{ot} sites, as shown in the four-, five-, and six-proton configurations in Figure 8. In an experimental scanning-tunneling microscopy (STM) study of H adsorption on RuO_2(110) Knapp et al.[28] also observed one and two protons bonded to O_{ot}, and one proton bonded to O_{br}, forming a hydrogen bond with a neighboring O_{ot}, as in Figure 8. Water formation on O_{br} was not observed, in agreement with the results obtained from DFT calculations.[15,27] In contrast, an X-ray diffraction study by Chu et al. proposed a low-voltage 1.5H/Ru structure with water on the O_{br} sites.[34] We find that if this suggested structure is used as a starting configuration for self-consistent GGA calculations, the bridging O retracts back into the surface and one of its protons is transferred to O_{ot}, resulting in the 1.5 H/Ru configuration shown in Figure 7. Our structure at 1 H/Ru coverage is similar to the medium voltage structure of Chu et al.,[34] except that they oriented the hydrogens perpendicular to the (110) plane. We predict that RuO_2(110) will deprotonate near the O_2 evolution voltage, while Chu et al. suggest a structure with an adsorbed water layer in close proximity of the surface. In our calculations, such a water layer is not stable and relaxes back away from the surface, severing all hydrogen bonds and resulting in a configuration of higher free energy than the O2 surface shown in Figure 7.

6. Models of Hydrous $RuO_2 \cdot xH_2O$

As explained in section 1, the structure of hydrous ruthenia is key for understanding its high performance in ECs. Two previously proposed structure models[3,11] are shown in Figure 1a and b, and will be referred to as as "water in bulk vacancies" and "water at grain boundaries", respectively. Here, we evaluate the relative energetic stability of these $RuO_2 \cdot xH_2O$ structure models by investigating structures

with one or two water molecules in bulk vacancies and structures where water aggregates in layers between slabs of crystalline RuO_2.

We define the hydration free energy of $RuO_2 \cdot xH_2O$ with respect to anhydrous RuO_2 and liquid water:

$$\Delta G = \frac{G[RuO_2 \cdot xH_2O] - G[RuO_2]}{x} - \mu_{H_2O} \qquad (8)$$

where μ_{H_2O} is the chemical potential of liquid water. While the free energies of $RuO_2 \cdot xH_2O$ and RuO_2 can be reasonably approximated by their DFT total energies, the free energy of water at ambient conditions is difficult to evaluate directly from first-principles calculations. Instead, we construct an estimate of μ_{H_2O} using a judicious combination of experimental data and DFT total energies. We consider a hydration reaction such as $CaO + H_2O(l) \rightarrow Ca(OH)_2$, which has a measured standard enthalpy of $\Delta H^\circ_{rxn} = -65.17$ kJ/mol.[35] This reaction resembles the hydration process described by eq 8 since CaO and $Ca(OH)_2$ are both bulk solids at 25 °C. From the calculated DFT total energies, $E[CaO]$ and $E[Ca(OH)_2]$, one can obtain an estimate of the free energy of water in its standard state at 25 °C to be used with the DFT energies of $RuO_2 \cdot xH_2O$ and Ru_2O:

$$\mu_{H_2O} = E[Ca(OH)_2] - E[CaO] - \Delta H^\circ_{rxn} - T^\circ S^\circ \qquad (9)$$

where $S^\circ = 69.95$ J/(mol K) is the standard state entropy of water at $T^\circ = 298.15$ K. We note that while the total energy of each phase individually can contain very large systematic errors, these errors should largely cancel out in taking the total energy differences in eqs 8 and 9. This prescription implicitly assumes that the vibrational free energy (including zero-point energy) of hydroxyl groups in $Ca(OH)_2$ approximately equals that of water in $RuO_2 \cdot xH_2O$. This is indeed the case: the frequencies of the vibrational modes of H_2O are 3657 and 3756 cm^{-1} for O−H stretching and 1595 cm^{-1} for H−O−H bending,[35] which together with the thermal energy of three rotational modes give 0.6 eV/H_2O. The corresponding frequencies of the O−H stretching modes in $Ca(OH)_2$ are 3620 and 3640 cm^{-1}, and the doubly degenerate librational frequencies are 373 and 680 cm^{-1},[36] resulting in a zero-point energy of $E_{vib}[(OH)_2] = 0.58$ eV. Tests show that choosing $Mg(OH)_2$ or KOH as the reference compounds leads to changes in μ_{H_2O} of only −4 and +29 meV, respectively, much smaller than the scale of the calculated hydration energies.

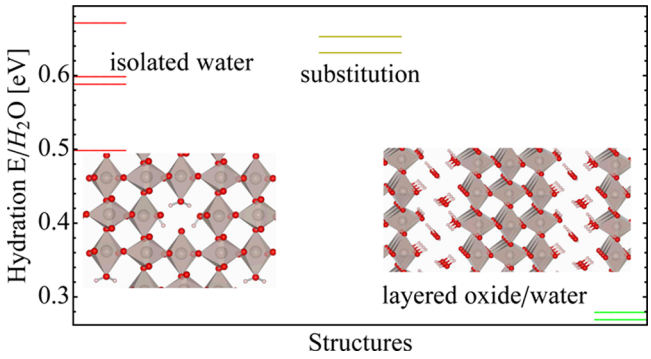

FIGURE 9. Structures and calculated hydration free energies for different models of $RuO_2 \cdot xH_2O$. Structures labeled "substitution" refer to hypothetical compounds $RuO(OH)_2$ and $Ru_2O_4 \cdot H_2O$ in the crystal structures of $VO(OH)_2$ and $V_2O_4 \cdot H_2O$.

We use PEGS to predict low-energy structure models of hydrous ruthenia. We vary the number of Ru vacancies; in each vacancy, we place four protons in the form of either two H_2O molecules or four OH^- groups. Global electrostatic energy minimization is carried out with respect to proton configurations, including which oxygen atoms to bond to and at what orientation, keeping all other ions fixed. The calculated hydration free energies [eq 8] of the low-energy structures with isolated or aggregate (layered) distributions of Ru vacancies are shown in Figure 9. PEGS finds that the favorable proton positions are always located around the Ru vacancy site since it naturally has a low electrostatic potential. Furthermore, protons are generally oriented toward the vacancy; see the left inset in Figure 9. For structures with an isolated Ru vacancy, the energy penalty to incorporate water into the bulk structure is high (approximately 0.5 eV/H_2O), strongly favoring phase separation into anhydrous RuO_2 and water. We have also searched the Inorganic Crystal Structure Database (ICSD)[37] for known structures of tetravalent metal hydroxides with the general formula $M_mO_nH_{2n-4m}$, encompassing hydrates, hydroxides, and oxyhydroxides. There are only two such compounds with completely determined hydrogen positions, $VO(OH)_2$ and $V_2O_4 \cdot H_2O$; the corresponding hydration energies for compounds where V is substituted by Ru are above 0.6 eV/H_2O. The tendency toward water aggregation is clearly evident in Figure 9, since the structures with a layered arrangement of Ru vacancies are much lower in energy than the bulk-incorporated structures, though still unstable by a sizable amount (approximately 0.26 eV/H_2O). Thus, DFT results suggest that the existence of homogeneous hydrous RuO_2

is unlikely and indirectly support the "water at grain boundaries" model of $RuO_2 \cdot xH_2O$.

7. Summary and Outlook

DFT calculations show that the intuitive picture where electron−proton double-insertion leads to a valence change from Ru^{4+} to Ru^{3+} should be treated with caution due to the metallic character and delocalized nature of the electronic states near the Fermi level of RuO_2. We find that the proton intercalation voltage in bulk RuO_2 is low (≈0.1 V) and the proton migration barrier is high (1.8 eV), suggesting that the charging rate-dependent diffusive contributions observed at low voltages (relative to RHE) are due to bulk intercalation and one-dimensional diffusion along the RuO_6 chains. An additional charge storage mechanism operates at higher voltages (0.3 to 1.2 V w.r.t. RHE) and involves reversible proton adsorption at surface oxygen sites to form hydroxyl and water groups, corresponding to coverages of up to 1.5 H/Ru. Theory also predicts that hydrous $RuO_2 \cdot xH_2O$ energetically favors structures where water aggregates at the grain boundaries between regions of crystalline RuO_2, indirectly supporting the "water at grain boundaries" structure model where intergranular water layers provide fast protonic conduction pathways and metallic RuO_2 nanocrystals facilitate rapid electronic transport.

So far, theory and experiments have only scratched the surface of the rich phenomena in hydrous nanostructured electrode materials, and this remains a fruitful area for future research in physics, chemistry, and materials science. Future studies could be aimed at understanding the detailed physical mechanisms associated with electron and proton transport and their relation to the atomic-level structure of the hydrous electrode. For instance, nuclear magnetic resonance studies in combination with DFT calculations could be used to further refine structure models of $RuO_2 \cdot xH_2O$, and studies of proton diffusion through the hydrous regions should provide insight into the low activation energies measured by neutron scattering.[10] Better structure models could also serve as the starting point for investigating electron transport across the structural water layer separating crystallites of anhydrous RuO_2, providing an in-depth understanding of the fundamental mechanisms and design rules for next-generation aqueous ECs.

This work was supported as part of the Molecularly Engineered Energy Materials, an Energy Frontier Research Center funded by the US Department of Energy, Office of Science, Basic Energy Sciences under Award Number DE-SC0001342, and by the UC Office of the President under MRPI Award "Next-Generation Supercapacitors".

BIOGRAPHICAL INFORMATION

Vidvuds Ozoliņš is Professor in the Department of Materials Science and Engineering at UCLA. He earned a Ph.D. in Theoretical Physics from the Royal Institute of Technology in Sweden in 1998. His research focuses on first-principles studies of materials for energy storage, generation, and conversion.

Fei Zhou graduated with a Ph.D. in Physics from Massachusetts Institute of Technology in 2006 and is currently a researcher in the Department of Materials Science and Engineering at UCLA. His research interests include the development of new approaches to studying materials for electrochemical energy storage and strongly correlated oxides.

Mark Asta is Professor and Chair in the Department of Materials Science and Engineering at UC Berkeley, where he received his PhD in 1993. His research focuses on the application of first-principles density-functional-theory and classical atomistic simulations to the study of the structure and properties of materials for advanced structural and energy applications.

FOOTNOTES

*To whom correspondence should be addressed. E-mail: vidvuds@ucla.edu.
The authors declare no competing financial interest.

REFERENCES

1 Winter, M.; Brodd, R. J. What Are Batteries, Fuel Cells, and Supercapacitors? *Chem. Rev.* **2004**, *104*, 4245–4270.
2 Kötz, R.; Carlen, M. Principles and applications of electrochemical capacitors. *Electrochim. Acta* **2000**, *45*, 2483–2498.
3 McKeown, D.; Hagans, P.; Carette, L.; Russell, A.; Swider, K.; Rolison, D. Structure of hydrous ruthenium oxides: Implications for charge storage. *J. Phys. Chem. B* **1999**, *103*, 4825–4832.
4 Sugimoto, W.; Yokoshima, K.; Murakami, Y.; Takasu, Y. Charge storage mechanism of nanostructured anhydrous and hydrous ruthenium-based oxides. *Electrochim. Acta* **2006**, *52*, 1742–1748.
5 Rolison, D. R.; Long, J. W.; Lytle, J. C.; Fischer, A. E.; Rhodes, C. P.; McEvoy, T. M.; Bourg, M. E.; Lubers, A. M. Multifunctional 3D nanoarchitectures for energy storage and conversion. *Chem. Soc. Rev.* **2009**, *38*, 226–252.
6 Over, H. Surface Chemistry of Ruthenium Dioxide in Heterogeneous Catalysis and Electrocatalysis: From Fundamental to Applied Research. *Chem. Rev.* **2012**, *112*, 3356–3426.
7 Trasatti, S.; Buzzanca, G. Ruthenium dioxide: A new interesting electrode material. Solid state structure and electrochemical behaviour. *J. Electroanal. Chem. Interfacial Electrochem.* **1971**, *29*, A1–A5.
8 Ardizzone, S.; Fregonara, G.; Trasatti, S. Inner and outer active surface of RuO_2 electrodes. *Electrochim. Acta* **1990**, *35*, 263–267.
9 Zheng, J. P.; Cygan, P. J.; Jow, T. R. Hydrous Ruthenium Oxide as an Electrode Material for Electrochemical Capacitors. *J. Electrochem. Soc.* **1995**, *142*, 2699–2703.
10 Fu, R.; Ma, Z.; Zheng, J. P. Proton NMR and Dynamic Studies of Hydrous Ruthenium Oxide. *J. Phys. Chem. B* **2002**, *106*, 3592–3596.
11 Dmowski, W.; Egami, T.; Swider-Lyons, K. E.; Love, C. T.; Rolison, D. R. Local Atomic Structure and Conduction Mechanism of Nanocrystalline Hydrous RuO_2 from X-ray Scattering. *J. Phys. Chem. B* **2002**, *106*, 12677–12683.
12 Sugimoto, W.; Iwata, H.; Yokoshima, K.; Murakami, Y.; Takasu, Y. Proton and Electron Conductivity in Hydrous Ruthenium Oxides Evaluated by Electrochemical Impedance Spectroscopy: The Origin of Large Capacitance. *J. Phys. Chem. B* **2005**, *109*, 7330–7338.
13 Hu, C.-C.; Chang, K.-H.; Lin, M.-C.; Wu, Y.-T. Design and Tailoring of the Nanotubular Arrayed Architecture of Hydrous RuO_2 for Next Generation Supercapacitors. *Nano Lett.* **2006**, *6*, 2690–2695.

14 Lin, K.-M.; Chang, K.-H.; Hu, C.-C.; Li, Y.-Y. Mesoporous RuO_2 for the next generation supercapacitors with an ultrahigh power density. *Electrochim. Acta* **2009**, *54*, 4574–4581.

15 Liu, Y.; Zhou, F.; Ozolins, V. Ab Initio Study of the Charge-Storage Mechanisms in RuO_2-Based Electrochemical Ultracapacitors. *J. Phys. Chem. C* **2012**, *116*, 1450–1457.

16 Sorantin, P. I.; Schwarz, K. Chemical bonding in rutile-type compounds. *Inorg. Chem.* **1992**, *31*, 567–576.

17 Bader, R.; Matta, C. Atoms in molecules as non-overlapping, bounded, space-filling open quantum systems. *Found. Chem.* **2012**, 1–24.

18 Stausholm-Moller, J.; Kristoffersen, H. H.; Hinnemann, B.; Madsen, G. K. H.; Hammer, B. DFT+U study of defects in bulk rutile TiO_2. *J. Chem. Phys.* **2010**, *133*, 144708.

19 Aydinol, M.; Kohan, A.; Ceder, G. Ab initio calculation of the intercalation voltage of lithium transition metal oxide electrodes for rechargeable batteries. *J Power Sources* **1997**, *68*, 664–668.

20 Chase, M. W.; Davies, C. A.; Downey, J. R.; Frurip, D.; McDonald, R.; Syverud, A. JANAF Thermochemical Tables, 3rd ed. *J. Phys. Chem. Ref. Data* 1985, *14*, Suppl. No. 1.

21 Majzoub, E. H.; Ozoliņš, V. Prototype electrostatic ground state approach to predicting crystal structures of ionic compounds: Application to hydrogen storage materials. *Phys. Rev. B* **2008**, *77*, 104115.

22 Majzoub, E. H.; Zhou, F.; Ozolins, V. First-Principles Calculated Phase Diagram for Nanoclusters in the Na-Al-H System: A Single-Step Decomposition Pathway for $NaAlH_4$. *J. Phys. Chem. C* **2011**, *115*, 2636–2643.

23 Wang, F.; Landau, D. Determining the density of states for classical statistical models: A random walk algorithm to produce a flat histogram. *Phys. Rev. E* **2001**, *64*, 056101.

24 Henkelman, G.; Uberuaga, B.; Jónsson, H. A climbing image nudged elastic band method for finding saddle points and minimum energy paths. *J. Chem. Phys.* **2000**, *113*, 9901.

25 Fermann, J.; Auerbach, S. Modeling proton mobility in acidic zeolite clusters: II. Room temperature tunneling effects from semiclassical rate theory. *J. Chem. Phys.* **2000**, *112*, 6787–6794.

26 Over, H.; Knapp, M.; Lundgren, E.; Seitsonen, A.; Schmid, M.; Varga, P. Visualization of atomic processes on ruthenium dioxide using scanning tunneling microscopy. *Chem. Phys. Phys. Chem.* **2004**, *5*, 167–174.

27 Reuter, K.; Scheffler, M. Composition, structure, and stability of RuO_2(110) as a function of oxygen pressure. *Phys. Rev. B* **2001**, *65*, 035406.

28 Knapp, M.; Crihan, D.; Seitsonen, A. P.; Lundgren, E.; Resta, A.; Andersen, J. N.; Over, H. Complex Interaction of Hydrogen with the RuO_2(110) Surface. *J. Phys. Chem. C* **2007**, *111*, 5363–5373.

29 Wang, H.; Schneider, W. F.; Schmidt, D. Intermediates and Spectators in O_2 Dissociation at the RuO_2(110) Surface. *J. Phys. Chem. C* **2009**, *113*, 15266–15273.

30 Lister, T.; Chu, Y.; Cullen, W.; You, H.; Yonco, R.; Mitchell, J.; Nagy, Z. Electrochemical and X-ray scattering study of well defined RuO_2 single crystal surfaces. *J. Electroanal. Chem.* **2002**, *524−525*, 201–218.

31 Zhou, F.; Cococcioni, M.; Marianetti, C. A.; Morgan, D.; Ceder, G. First-principles prediction of redox potentials in transition-metal compounds with LDA+U. *Phys. Rev. B* **2004**, *70*, 235121.

32 Anisimov, V. I.; Zaanen, J.; Andersen, O. K. Band theory and Mott insulators: Hubbard U instead of Stoner I. *Phys. Rev. B* **1991**, *44*, 943–954.

33 Norskov, J. K.; Rossmeisl, J.; Logadottir, A.; Lindqvist, L.; Kitchin, J. R.; Bligaard, T.; Jónsson, H. Origin of the Overpotential for Oxygen Reduction at a Fuel-Cell Cathode. *J. Phys. Chem. B* **2004**, *108*, 17886–17892.

34 Chu, Y.; Lister, T.; Cullen, W.; You, H.; Nagy, Z. Commensurate Water Monolayer at the RuO_2(110)/Water Interface. *Phys. Rev. Lett.* **2001**, *86*, 3364–3367.

35 Chase, M. W., Jr. NIST-JANAF Themochemical Tables, Fourth Edition *J. Phys. Chem. Ref. Data* Monograph 9, 1998, 1−1951.

36 Lutz, H.; Moller, H.; Schmidt, M. Lattice Vibration-Spectra. 82. Brucite-Type Hydroxides $M(OH)_2$ (M = Ca, Mn, Co, Fe, Cd) - IR and Raman-Spectra, Neutron-Diffraction of $Fe(OH)_2$. *J. Mol. Struct.* **1994**, *328*, 121–132.

37 Belsky, A.; Hellenbrandt, M.; Karen, V.; Lucksh, P. New developments in the Inorganic Crystal Structure Database (ICSD): accessibility in support of materials research and design. *Acta Crystallogr. B* **2002**, *58*, 364–369.